Inorganic Chemistry
Article
pubs.acs.org/IC

Band Gap Engineering of ZnO using Core/Shell Morphology with Environmentally Benign Ag_2S Sensitizer for Efficient Light Harvesting and Enhanced Visible-Light Photocatalysis

Sunita Khanchandani,*[†] Pawan Kumar Srivastava,[‡] Sandeep Kumar,[†,§] Subhasis Ghosh,[‡] and Ashok K. Ganguli*[†,∥]

[†]Department of Chemistry, Indian Institute of Technology, Hauz Khas, New Delhi 110016, India
[‡]School of Physical Sciences, Jawaharlal Nehru University, New Delhi 110067, India
[§]Department of Chemistry, University of Delhi, Delhi 110007, India
[∥]Institute of Nano Science & Technology, Habitat Centre, Phase X, Sector 64, Mohali, Punjab 160062, India

Supporting Information

ABSTRACT: Band gap engineering offers tunable optical and electronic properties of semiconductors in the development of efficient photovoltaic cells and photocatalysts. Our study demonstrates the band gap engineering of ZnO nanorods to develop a highly efficient visible-light photocatalyst. We engineered the band gap of ZnO nanorods by introducing the core/shell geometry with Ag_2S sensitizer as the shell. Introduction of the core/shell geometry evinces great promise for expanding the light-harvesting range and substantial suppression of charge carrier recombination, which are of supreme importance in the realm of photocatalysis. To unveil the superiority of Ag_2S as a sensitizer in engineering the band gap of ZnO in comparison to the Cd-based sensitizers, we also designed ZnO/CdS core/shell nanostructures having the same shell thickness. The photocatalytic performance of the resultant core/shell nanostructures toward methylene blue (MB) dye degradation has been studied. The results imply that the ZnO/Ag_2S core/shell nanostructures reveal 40- and 2-fold enhancement in degradation constant in comparison to the pure ZnO and ZnO/CdS core/shell nanostructures, respectively. This high efficiency is elucidated in terms of (i) efficient light harvesting owing to the incorporation of Ag_2S and (ii) smaller conduction band offset between ZnO and Ag_2S, promoting more efficient charge separation at the core/shell interface. A credible photodegradation mechanism for the MB dye deploying ZnO/Ag_2S core/shell nanostructures is proposed from the analysis of involved active species such as hydroxyl radicals ($OH^\bullet$), electrons (e^-_{CB}), holes (h^+_{VB}), and superoxide radical anions ($O_2^{\bullet -}$) in the photodegradation process utilizing various active species scavengers and EPR spectroscopy. The findings show that the MB oxidation is directed mainly by the assistance of hydroxyl radicals ($OH^\bullet$). The results presented here provide new insights for developing band gap engineered semiconductor nanostructures for energy-harvesting applications and demonstrate Ag_2S to be a potential sensitizer to supersede Cd-based sensitizers for eco-friendly applications.

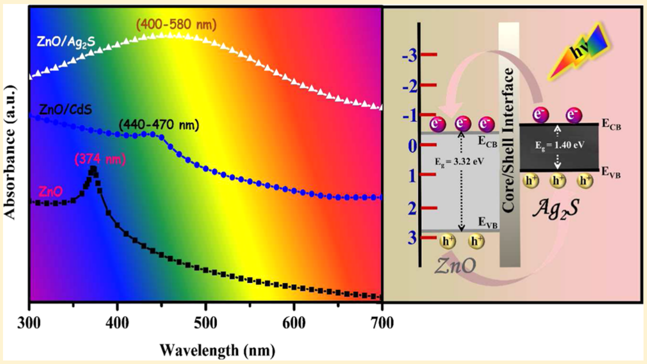

INTRODUCTION

With the advent of industrialization, the pursuit of environmental pollution abatement has remained a pivotal endeavor.[1] Among the copious abatement strategies known, semiconductor photocatalysis has garnered intense scrutiny as a potential solution to the sustainable development of energy resources and for ameliorating the environment.[2,3] Attention to date has focused largely on TiO_2 as the archetypal photocatalyst, since it is conferred with high surface-to-volume ratio and admirable physiochemical properties.[4−6] However, several recent studies have addressed the possibility of using an alternative to TiO_2. ZnO is being perceived as a potential alternative to TiO_2 since it unveils band gaps and physical properties similar to those of TiO_2.[7−9] Importantly, ZnO has outstanding electron mobility and longer lifetime of charge carriers in comparison to TiO_2, which would help to achieve enhanced photocatalytic degradation of the dye.[10] Another important advantage of ZnO over TiO_2 is that it is amenable to a range of fabrication procedures such as sol-gel processes, chemical bath deposition, and electrodeposition, which allows greater optimization of morphology than is possible for TiO_2.[11] However, despite those good attributes of ZnO, three formidable challenges still remain. One centers on rapid

Received: March 5, 2014
Published: August 21, 2014

recombination of charge carriers of ZnO, which greatly reduces its photocatalytic efficiency.[9] A second entails its wide band gap, which severely precludes the employment of visible light accounting for 43% of the solar spectrum.[12a] The third posts the congenital impediment of photocorrosion, which greatly curtails its photocatalytic activity and photostability.[12b] Thus, on account of these perennial issues, attempts have been made to engineer the band gap of ZnO for efficient separation of charges and enhanced photocatalytic efficiency in the visible region. In this regard, an appealing approach to customize the optical properties of materials is through the control of dimensions on a nanoscale. In contrast with zero-dimensional (0D) nanoparticulate motifs, 1D nanostructures such as nanotubes, nanobelts, nanowires, and nanorods represent an exciting and promising structural paradigm with their inherent large specific surface areas and the prospect of enhanced light trapping and thus, in turn, benefits in solar energy harvesting.[13,14] Anchoring low band gap semiconductors such as CdS, PbS, InP, Bi_2S_3, Sb_2S_3, and CdSe on large band gap semiconductors is another alluring strategy to maximize the absorption of incident photons.[15−20] Inorganic low band gap semiconductors have gained acceptance as sensitizers across a broad spectral range from visible to infrared, benefiting from the ability to tune the optical properties by modulating size and composition, offering high extinction coefficient and delivering longer lifetimes of excitons and the notable property of generation of mutilple excitons per absorbed photon. CdSe and CdS nanoparticles, in particular, have been extensively employed in photocatalysis and in boosting the efficiency of photovoltaic cells as sensitizers, credited to the enhanced light-harvesting ability and the apposite band gap configuration with the metal oxide ensuring efficient collection and transportation of charge carriers.[21,22] Following the utilization of these Cd-based sensitizers, current efforts have ensued with remarkable achievements of up to 99.0% photocatalytic efficiency and 12.3% energy conversion efficiency.[23,24] While incredible breakthroughs have been accomplished, utilizing the Cd-based sensitizers imposes environmental concerns, stemming from the detrimental impact and the strict environmental regulations in several countries to alleviate Cd input into the environment. To surmount these potential issues, the quest for environmentally friendly sensitizers is imperative for clean, efficient, sustainable, and safe utilization of semiconductor nanostructures. To move toward this goal, here we select Ag_2S, a narrow band gap semiconductor, owing to its outstanding properties. Its narrow band gap (~1 eV), high absorption coefficient, good chemical stability, and biocompatibility have favored the use Ag_2S in photovoltaics, photocatalysis, and bioimaging agents. Ag_2S evinces an ultralow solubility product constant ($K_{sp} = 6.3 \times 10^{-50}$), which guarantees that the least amount of Ag^+ ion is released into the biological surroundings.[25] Additional levels of improvement in photocatalytic efficiency could be achieved through implementation of a core/shell strategy,[26] which results in a potential barrier between the core and the shell, thereby suppressing the charge carrier recombination. The emergence of the Ag_2S shell onto the ZnO nanorod cores gives a type II system of the core/shell nanostructures which offers a scaffold for suppressing the charge carrier recombination at the core/shell interface. Thus, the implementation of ZnO and Ag_2S in a core/shell morphology suppresses the charge carrier recombination and renders remarkably enhanced visible-light-driven photocatalysis ensuing through the onset of type II band gap configuration.[27,28]

On the basis of the above considerations, we intend to fabricate ZnO/Ag_2S core/shell nanostructures which could be a potential alternative to Cd-based sensitizers for meeting the clean energy demand. In the current study, we synthesized a Ag_2S shell on ZnO nanorods using a facile surface-functionalization method. ZnO/Ag_2S core/shell nanorods were utilized as photocatalysts in the degradation of methylene blue (MB) because they purvey a continuous pathway for charge carrier collection and transportation ensuing through the benefits associated with one-dimensional structures. Due to the inherently low energy gap of Ag_2S, the resultant ZnO/Ag_2S core/shell nanorods exhibited enhanced light-harvesting capability and increased photocatalytic efficiency to degrade MB in comparison to the ZnO/CdS core/shell nanorods. These results offer Ag_2S as a potential sensitizer to supersede Cd-based sensitizers for eco-friendly applications.

■ EXPERIMENTAL SECTION

Synthesis of ZnO/Ag_2S and ZnO/CdS Core/Shell Nanorods. Taking into consideration the ability of citric acid[29] to bind to a variety of surfaces, we have used citric acid as the surface-modifying ligand for the growth of a shell (Ag_2S or CdS) on the ZnO nanorods[30] (synthesized using thermal decomposition of zinc acetate dihydrate). This method entails the functionalization of ZnO nanorods utilizing citric acid to achieve a stable dispersion and the ensuing dropwise addition of $AgNO_3$ or $Cd(NO_3)_2 \cdot 4H_2O$ and $Na_2S \cdot 9H_2O$ solution under constant magnetic stirring. Using $AgNO_3$ and $Na_2S \cdot 9H_2O$ precursors, the product obtained was black, indicative of the presence of Ag_2S along with ZnO nanorods. A yellow product was formed with the addition of $Cd(NO_3)_2 \cdot 4H_2O$ and $Na_2S \cdot 9H_2O$ solution, confirming the formation of CdS together with the ZnO nanorods. The resultant nanostructures were recovered through centrifugation and washed using deionized water and alcohol repeatedly to eliminate the possible impurities and subsequently dried at room temperature.

There is no potential hazard associated with the reported experimental work, however, the use of $Cd(NO_3)_2 \cdot 4H_2O$ and $Na_2S \cdot 9H_2O$ may cause mild skin irritation and thus care should be taken to avoid skin contact with them.

Synthesis of Shell Materials (Ag_2S or CdS) from the Core/Shell Nanostructures. Following the fact that ZnO is soluble in dilute mineral acids, Ag_2S or CdS shells were obtained by detaching the inner ZnO core from the ZnO/Ag_2S or ZnO/CdS core/shell nanostructures in dilute HCl solution (as shown in Figure S1, Supporting Information).

Characterization. *Powder X-ray Diffraction (PXRD).* A detailed understanding of the crystallinity and phase purity of the resultant samples was procured by utilizing powder XRD with a Bruker D8 Advance powder X-ray diffractometer, functioning in the Bragg arrangement using Ni-filtered Cu Kα radiation ($\lambda = 0.15418$ nm). The resultant samples were thoroughly grounded using a mortar and pestle for analysis. Powder diffraction patterns were acquired in the 2θ range of 20−70° at a scan rate of 0.3°/min and using 0.02° as the step size. During the scans, the parameters employed for slit width and accelerating voltage were uniform for all of the resultant samples. PXRD analysis was used to estimate the crystallite sizes and the lattice strain in samples. Crystallite sizes (D) were obtained through the implementation of the Scherrer relation (eq 1) to the PXRD data.

$$D = K\lambda/\beta \cos\theta \quad (1)$$

where λ represents the wavelength of the incident X-rays, β represents the width of the X-ray diffraction peak in radians (full width at half-maximum), θ represents the Bragg angle in radian,s and K represents the shape factor (taken as 0.9).

To estimate the lattice strain Williamson and Hall method (eq 2)[31] was used.

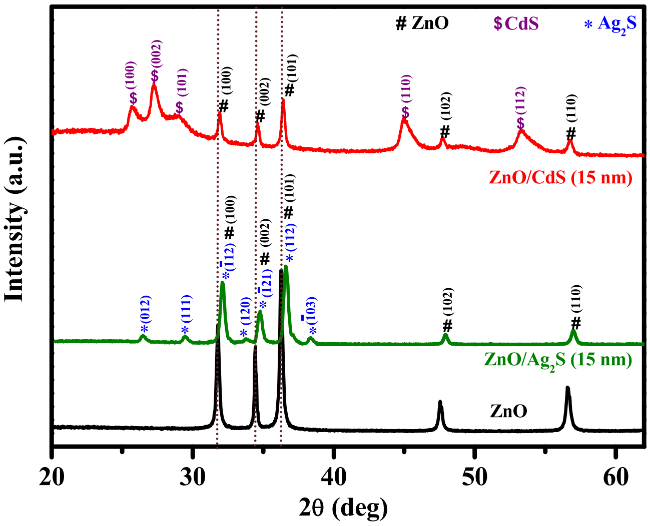

Figure 1. Powder X-ray diffraction patterns of uncoated ZnO nanorods and ZnO/Ag_2S and ZnO/CdS core/shell nanostructures.

$$\beta \cos \theta/\lambda = 1/D + \eta \sin \theta/\lambda \qquad (2)$$

where β represents width of X-ray diffraction peak in radians (full-width at half-maxima), θ represents Bragg angle in radians, λ represents wavelength of the incident X-rays, D represents size of the crystallites and η represents effective lattice strain. A curve that plots $\beta \cos \theta/\lambda$ on the y axis and $\sin \theta/\lambda$ on the x axis is drawn. The slope and intercept of a plot of $\beta \cos \theta/\lambda$ versus $\sin \theta/\lambda$ permit the estimation of strain and crystallite size, respectively.

Electron Microscopy. At the outset, the diameters and lengths of the resultant nanostructures were characterized utilizing the assistance of a JEOL, JSM-6700F field-emission scanning electron microscope (FESEM), functioning at an accelerating voltage of 5 kV.

Samples for FESEM analysis were fabricated through drop-casting an ultrasonicated dispersion of the resultant samples in ethanol on the surfaces of FESEM brass stubs using conductive carbon tape and subsequently subjected to sputter coating with a layer of gold, so as to lessen the sample charging effects.

Transmission electron microscopy (TEM) and high-resolution transmission electron microscopy (HRTEM) studies were engaged to achieve exhaustive insights into the morphology of the resultant nanostructures. Samples for TEM measurements were obtained by dispersing the resultant nanostructures in ethanol under the aid of ultrasonication and subsequently drying droplets of the suspension onto a holey carbon-coated 300-mesh Cu grid. Images were acquired on a JEOL 2010F functioned at a 200 kV accelerating voltage. The TEM was coupled with an energy dispersive spectroscopy (EDS) detector with the ability to acquire EDS elemental mapping to further validate the core/shell geometry in ZnO/CdS and ZnO/Ag_2S nanostructures.

Ultraviolet−Visible (UV−Vis) Absorption Spectra. UV−visible absorption spectra of the resultant nanostructures were assessed on a UV-2401 PC Shimadzu spectrophotometer employing 1 cm optical path length quartz cells. The resultant samples were mixed with ethanol under sonication for 5 min to give dispersions. The ethanolic dispersion of the nanostructured powder was placed in a quartz cuvette, and the cuvette was gradually shaken before recording each spectrum. Ethanol was utilized as a solvent owing to its low UV cutoff value (205 nm).

Photocatalysis Test. A heterocyclic aromatic dye, methylene blue (MB), was appointed as the evocative organic pollutant to explore the photocatalytic performance of the resultant nanostructures under illumination of visible light at ambient temperature and pressure. The visible-light-driven photocatalytic tests were executed in a 100 mL glass beaker. To induce visible light, a 500 W xenon lamp, provided with cutoff filter ($\lambda \geq 420$ nm), was placed about 5 cm away from the beaker (the intensity of the light employed was 100 mW cm^{-2}). Typically, in a visible-light-driven photocatalytic test, 20 mg of the resultant nanostructures (catalyst) was suspended in 80 mL of an aqueous solution of MB (of 1.0×10^{-5} M) to achieve the catalyst suspension. The catalyst suspension was stirred magnetically in the dark for 12 h to ensure the complete equilibration of absorption/desorption between the catalyst and MB prior to illumination. Requisite aliquots (4 mL) were withdrawn periodically and centrifuged to separate the residual catalyst particulates. The photocatalytic performance was scrutinized by observing the absorbance of the characteristic peak of MB at 660 nm utilizing a UV-2401 PC Shimadzu spectrophotometer. The degradability of MB is depicted by C/C_0, where C_0 and C denote the absorbance of the characteristic peak of MB at 660 nm before and after illumination.

Analysis of the Photocatalysis Mechanism. To gain a deeper insight into the mechanistic pathway of photocatalysis, controlled photocatalytic activity experiments utilizing various active species scavengers were realized analogous to the above photodegradation of MB deploying ZnO/Ag_2S core/shell catalysts, except that the radical scavengers (0.1 mmol) were injected into the reaction system. Photogenerated holes scavenger (ammonium oxalate), electrons scavenger ($AgNO_3$), superoxide radical anions scavenger (benzoquinone) and hydroxyl radicals scavenger (*tert*-butyl alcohol) were injected in the reaction system to probe the ruling contributor engaged in the photocatalytic degradation of MB.

Electron Paramagnetic Resonance (EPR) Spectroscopy. EPR spectroscopy employing the spin traps 5,5-dimethyl-1-pyrroline *N*-oxide (DMPO) was utilized to substantiate the possible involvement of $OH^{\bullet}$ and $O_2^{\bullet-}$ in the degradation of MB deploying ZnO/Ag_2S core/shell nanostructures under illumination of visible light and to further support the findings of the active species scavenger studies. Aqueous suspensions of ZnO/Ag_2S core/shell nanostructures and the spin trap (DMPO) were inserted into a quartz cell using a syringe. The quartz cell was subsequently positioned in the EPR cavity. The EPR spectra were recorded on a Bruker EPR 100d X-band spectrometer before and after illumination through the EPR cavity. A 500 W Xe lamp, the light source utilized in the photocatalytic test, was utilized as the irradiation source in EPR measurements. The parameters utilized in EPR measurements were as follows: center field, 3512 G; frequency, 9.74 GHz; microwave power, 20 mW.

■ RESULTS AND DISCUSSION

The optimized conditions for obtaining ZnO/CdS and ZnO/Ag_2S core/shell nanostructures were achieved by modulating the cadmium, silver, and sulfur precursor concentrations as well as by utilizing the varying concentrations of surface-functionalizing agent, citric acid (CA). The results achieved by optimizing the experimental parameters for the ZnO/Ag_2S

and ZnO/CdS core/shell nanostructures are discussed here. The absorption and photocatalytic studies clearly unravel the superiority of Ag_2S as an efficient sensitizer to sensitize wide band gap semiconductors and has the potential to supersede Cd-based sensitizers for eco-friendly applications.

Structural Characterization. To identify the structure and the phase purity of the resultant products, we had performed powder X-ray diffraction (PXRD) studies. Figure 1 presents the powder X-ray diffraction patterns of ZnO and ZnO/Ag_2S and ZnO/CdS core/shell systems. X-ray reflections of the pure ZnO nanostructures correlate closely with the wurtzite phase (hexagonal) of ZnO (JCPDS: 36-1451). The additional reflections observed at 26.45° (012), 29.44° (111), 33.89° (120), and 38.37° $(\bar{1}03)$ in the PXRD patterns of ZnO/Ag_2S core/shell nanostructures are undoubtedly indexed to the monoclinic phase of Ag_2S shell (JCPDS: 14-0072). In the PXRD patterns of ZnO/CdS core/shell nanorods, the reflections at 25.56° (100), 27.24° (002), 28.93° (101), 45.21° (110), and 53.62° (112) are well-indexed with CdS (JCPDS: 41-1049). The crystallographic phase of the synthesized ZnO/CdS core/shell system is confirmed as hexagonal for the CdS shell along with the hexagonal wurtzite for the ZnO core.

A closer look at the PXRD patterns of the ZnO/Ag_2S and ZnO/CdS core/shell nanostructures unfolds the effect of shell growth on ZnO. The emergence of the shell accentuates strain on ZnO, and PXRD provides a means to observe the strain induced by the core/shell formation. All of the reflections corresponding to ZnO shift to higher angles with the growth of the shell. Following the Bragg relation, the discerned shift of the reflections to higher angles results from the lattice contraction of the ZnO core upon shell growth. This implies that the emergence of the shell (Ag_2S and CdS) compresses the lattice planes of the core (ZnO) and reduces the lattice constant of ZnO in ZnO/CdS and ZnO/Ag_2S core/shell nanostructures in comaprison to the uncoated ZnO nanostructures, resulting in a gradual shift of the ZnO reflections to higher 2θ values in the ZnO core/shell nanostructures and implying the existence of lattice strain induced due to shell growth (Table 1).[32]

Table 1. Parameters Obtained from PXRD Investigation of ZnO and ZnO/Ag_2S and ZnO/CdS Core/Shell Nanostructures

		crystallite size (nm)			
sample	shell thickness (nm)	Scherrer eq	Williamson and Hall method	cell param (Å)	lattice strain (%)
ZnO		32.6	33.4	a = 3.254(2), c = 5.216(4)	+0.334
ZnO/Ag_2S	15	25.8	26.0	a = 3.248(2), c = 5.209(3)	−0.652
ZnO/CdS	15	26.4	26.5	a = 3.250(3), c = 5.212(4)	−0.521

To estimate the lattice strain induced in ZnO due to shell growth from the powder X-ray diffraction patterns, we have used the Williamson and Hall method.[31] A positive slope of the Williamson−Hall (W-H) plot signifies tensile strain, and a negative slope signifies compressive strain. Figure 2a illustrates a plot of $\beta \cos \theta/\lambda$ versus $\sin \theta/\lambda$ for uncoated ZnO (following eq 2), and the slope obtained is +0.0033. This tensile strain in ZnO is expected to manifest itself during the preparation method. The crystallite size obtained from the intercept is perceived to be 33.4 nm, which is in good accord with the calculated value of 32.6 nm following the Scherrer relation (Table 1). Figure 2b,c displays W−H plots for ZnO/Ag_2S and ZnO/CdS core/shell nanorods, respectively. The reversal of lattice strain is observed for the core/shell system, and the crystallite size obtained from the W−H plot is in accord with the calculated value from the Scherrer relation (Table 1). The presence of compressive strain indicates that the growth of the shell compresses the lattice planes in the core (ZnO). Importantly, the lattice strain at the core/shell interface is slightly larger for the ZnO/Ag_2S nanostructures (−0.652%) in comparison to the ZnO/CdS nanostructures (−0.521%). This difference is likely due to the lattice mismatch between the ZnO core (hexagonal) and Ag_2S shell (monoclinic). Thus, PXRD investigations clearly show the presence of a two-phase composition in the core/shell system, i.e., a hexagonal phase of ZnO and CdS and a monoclinic phase of Ag_2S along with a hexagonal phase of ZnO in ZnO/CdS and ZnO/Ag_2S nanorods, respectively, and also shed some light on evidence for the formation of a shell on the ZnO nanorods using Williamson−Hall analysis.

The synthesis of the shell materials (Ag_2S and CdS) is supported by the PXRD patterns shown in Figure S2 (Supporting Information).

Morphological Characterization. In order to investigate the bulk morphology and surface features of the samples, we have carried out field-emission scanning electron microscopy (FESEM), and the results are shown in Figure 3. As shown in Figure 3a, the obtained ZnO has rod-type morphology disclosing the length ranging from 500 to 600 nm and a uniform diameter of about 100 nm with smooth surfaces. However, subsequent to the emergence of the shell, ZnO nanorods have rougher surfaces (Figure 3b,c). Close observation of the nanorods in Figure 3b,c reveals that the secondary Ag_2S and CdS nanoparticles grow on the primary ZnO nanorods.

Further information about the core/shell nanostructures is procured by utilizing transmission electron microscopy (TEM). TEM analysis gives convincing evidence of the formation of a shell on the ZnO nanorods. Figure 4a manifests the TEM image of ZnO nanorods, and the inset shows the magnified image of an individual ZnO nanorod before the introduction of the shell. The bare ZnO nanorods exhibit a smooth surface and average diameter of 100 ± 7 nm. Following the shell growth, the diameter of ZnO nanorods has increased. A typical TEM image of the resultant ZnO/Ag_2S and ZnO/CdS core/shell nanorods is shown in Figure 4b,c, respectively. The brightness contrast between the core (dark) and the shell (light) indicates the formation of a core/shell geometry in the ZnO/Ag_2S and ZnO/CdS systems, as evident from Figure 4b,c. Considering that the increase in the diameter of nanorods with the growth of the shell is equal to the shell thickness counterpart (Ag_2S and CdS), the shell thickness was computed to be 15 nm. Thus, the TEM observations clearly indicate the formation of core/shell nanostructures with nearly the same shell thickness (Ag_2S and CdS; 15 nm). Additional persuasive evidence for the core/shell formation in ZnO/Ag_2S and ZnO/CdS nanostructures is revealed by HRTEM studies and EDS elemental mapping results. Presented in Figure 4d is a HRTEM of ZnO/Ag_2S core/shell nanostructures. From the analysis of the core/shell interface in HRTEM acquired through the specified rectangular section of ZnO/Ag_2S nanostructures (as marked in Figure 4b),

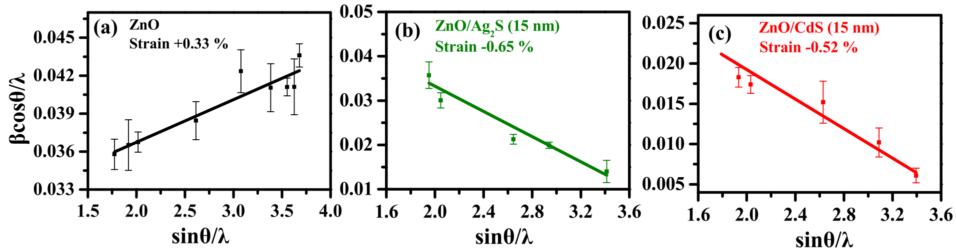

Figure 2. Williamson-Hall plots for (a) uncoated ZnO nanorods and (b) ZnO/Ag_2S and (c) ZnO/CdS core/shell nanostructures.

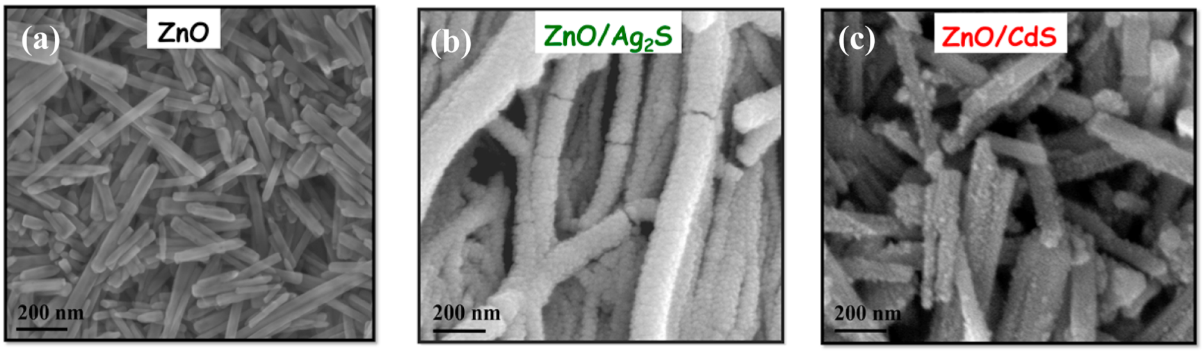

Figure 3. FESEM images of (a) uncoated ZnO nanorods and (b) ZnO/Ag_2S and (c) ZnO/CdS core/shell nanostructures.

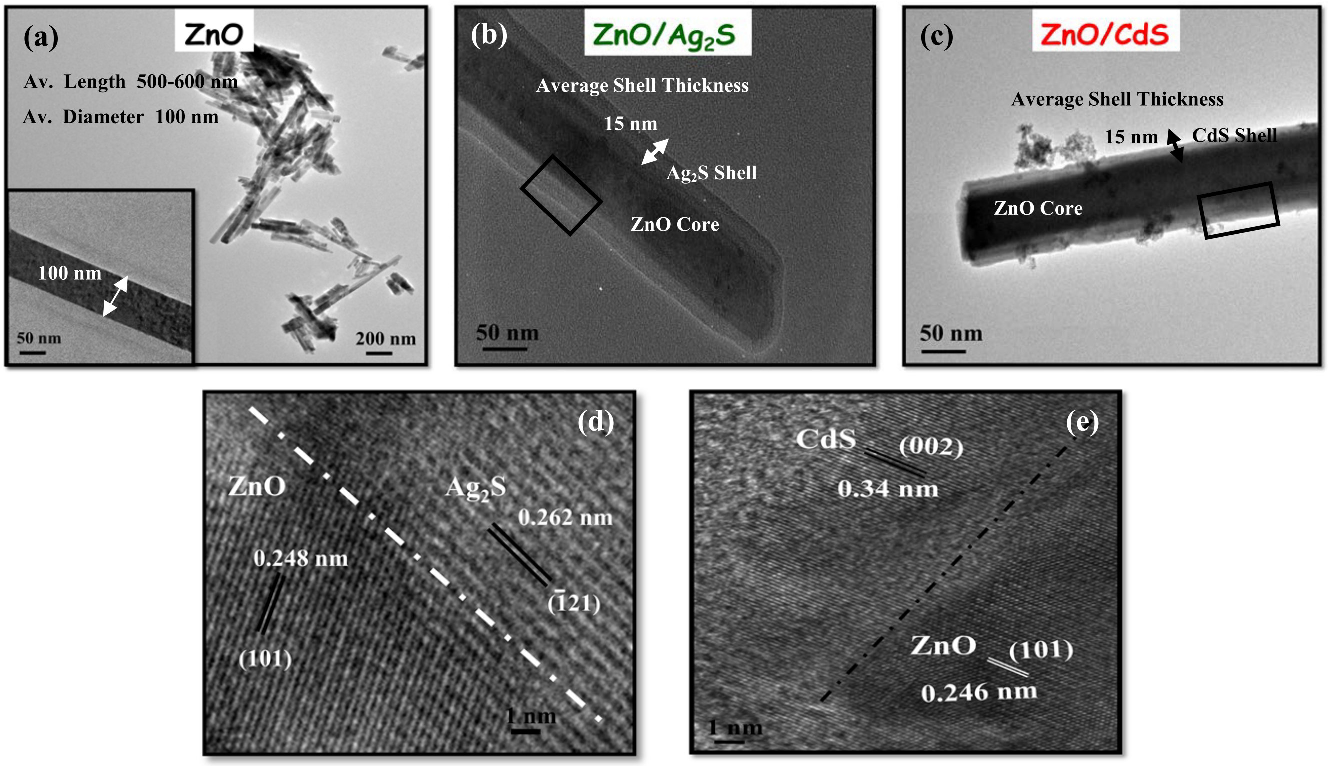

Figure 4. TEM images of (a) uncoated ZnO nanorods and (b) ZnO/Ag_2S and (c) ZnO/CdS core/shell nanostructures and HRTEM from the core/shell interface of (d) ZnO/Ag_2S and (e) ZnO/CdS nanostructures.

we discern that the ZnO/Ag_2S core/shell system reveals two sets of lattice fringes with spacings of 0.248 and 0.262 nm, correlating to the (101) plane of hexagonal ZnO and ($\bar{1}$21) plane of the monoclinic phase of Ag_2S, respectively, which clearly shows the simultaneous presence of ZnO and Ag_2S crystal lattices in the region of the interface. Similar kinds of results were obtained by the HRTEM studies of ZnO/CdS nanostructures depicted in Figure 4e (lattice fringe spacings of 0.34 and 0.246 nm were obtained correlating to (002) and (101) planes of CdS and ZnO, respectively), corroborating the formation of a core/shell type geometry in ZnO/CdS nanostructures.

Additional support for ZnO existing in the core and the shell being comprised of CdS or Ag_2S was ultimately furnished

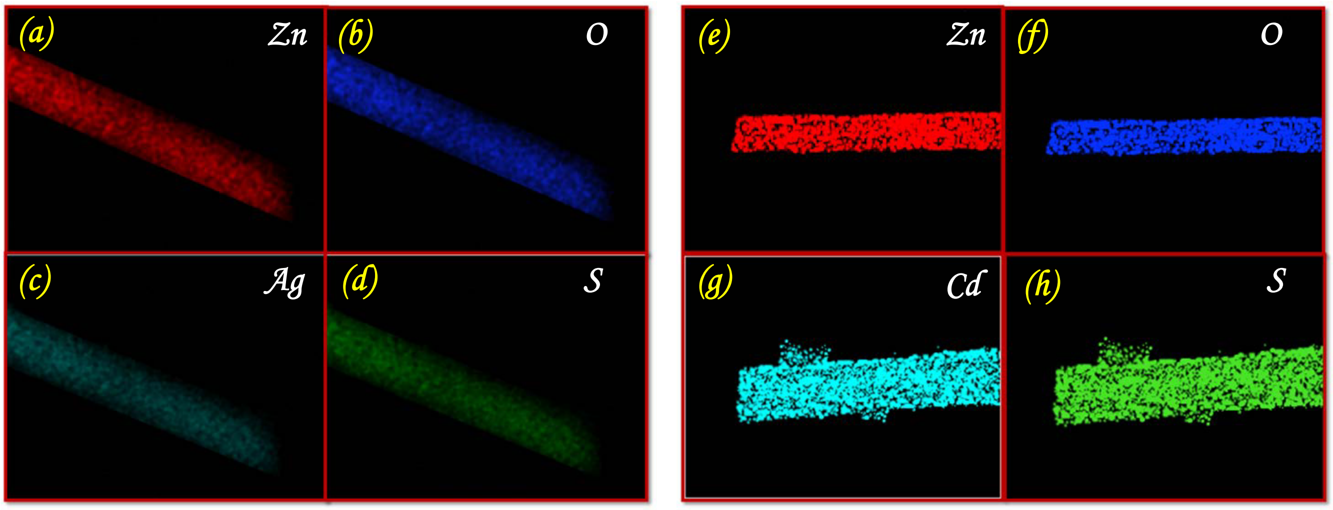

Figure 5. EDS elemental mapping of (a–d) ZnO/Ag_2S and (e–h) ZnO/CdS core/shell nanostructures.

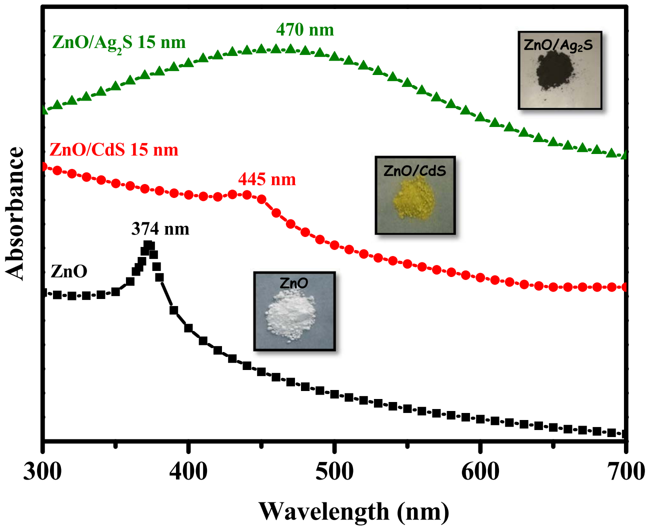

Figure 6. Optical absorption spectra of uncoated ZnO nanorods and ZnO/Ag_2S and ZnO/CdS core/shell nanostructures.

through EDS elemental mapping results. To decipher the composition of elements and the diameter of elemental distribution existing in ZnO/Ag_2S or CdS core/shell nanostructures, elemental mapping was performed. The results of elemental mapping (Figure 5a–d) of the ZnO/Ag_2S core/shell nanostructures (shown in Figure 4b) distinctly illustrated the coexistence of Zn, O, Ag, and S elements in the nanostructures. Apparently, all of the elements reveal uniform and homogeneous distribution; however, the distribution of Ag and S elements manifests a larger diameter in comparison to the other elements, underpinning that ZnO nanorods (core) are densely and uniformly encrusted by Ag_2S (shell) and unambiguously substantiating the core/shell geometry of the resultant ZnO/Ag_2S core/shell nanostructures. Likewise, the EDS elemental mapping of ZnO/CdS nanostructures in Figure 5e–h identifies the presence of Zn, O, Cd, and S elements and reveals greater diameters for shell elements (Cd and S), further substantiating the core/shell formation in ZnO/CdS nanostructures.

Thus, the combined techniques of TEM, HRTEM, and EDS elemental mapping observations makes it viable to unequivocally infer the core/shell geometry of ZnO/Ag_2S and ZnO/CdS nanostructures.

Optical Absorption Properties. To study the light-harvesting ability of the bare ZnO nanorods and the core/shell nanostructures, we performed UV–vis–NIR absorption spectroscopy. The signature of shell growth (Ag_2S and CdS) on the ZnO nanorods (core) could also be obtained from the UV–vis absorption spectrum. A shift of the absorption edge of ZnO at 374 nm to longer wavelengths and the broadening of the absorption spectra is observed with the growth of a shell (Ag_2S or CdS) on the ZnO core, as shown in Figure 6. The longer wavelength absorption and observed broadening of the absorption spectra upon shell growth can be explained by the type II electronic structures of the core/shell nanostructures, which enable the spatial separation of the photogenerated carriers and result in the electron wave function mainly residing in the ZnO core and the hole wave function localizing in the shell (Ag_2S or CdS).[33] The absorption profiles of ZnO/CdS and ZnO/Ag_2S core/shell nanostructures show the absorption onsets at 445 and 470 nm, respectively (shown in Figure 6), indicating that, for the same thickness of the shell, Ag_2S could harvest more light in comparison to CdS, owing to its narrow

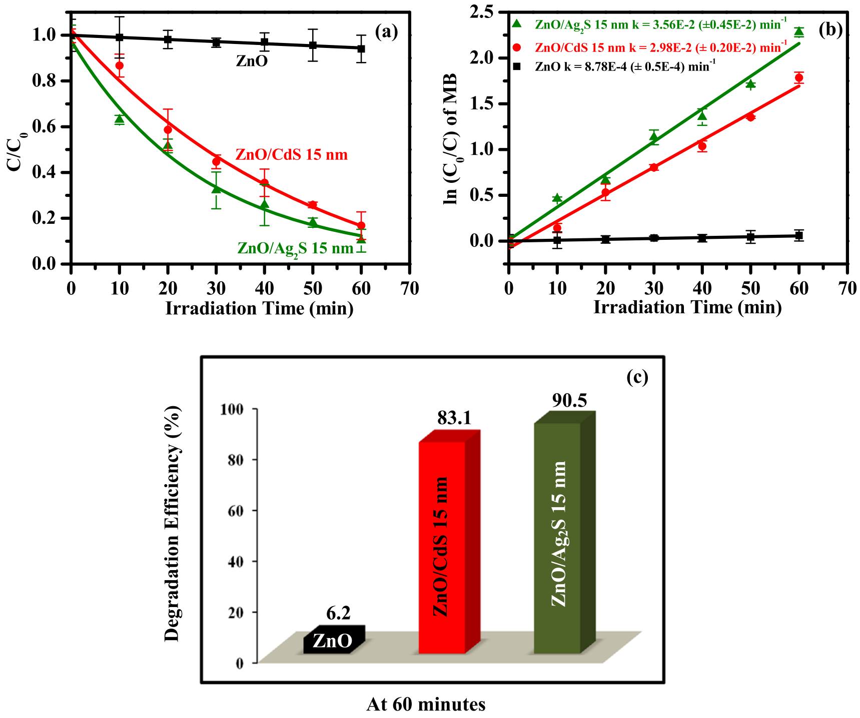

Figure 7. (a) Photocatalytic performances of uncoated ZnO nanorods and ZnO/Ag_2S and ZnO/CdS core/shell nanostructures for the degradation of MB solution under illumination of visible light, (b) plot of $\ln(C_0/C)$ as a function of visible irradiation time for photocatalysis of MB solution containing: uncoated ZnO nanorods and ZnO/Ag_2S and ZnO/CdS core/shell nanostructures, and (c) degradation efficiency of uncoated ZnO nanorods and ZnO/Ag_2S and ZnO/CdS core/shell nanostructures on the photodegradation of MB as a function of time. Experimental conditions: intensity of light used 100 mW cm^{-2}, wavelength of incident light 420−800 nm, amount of the photocatalyst taken 20 mg in 80 mL of 1×10^{-5} M MB aqueous solution, and 500 W xenon lamp as the light source.

band gap. The light-harvesting ability is also discernible from the photographs of the synthesized nanostructures, incorporated in the inset of Figure 6. The samples with Ag_2S coating appear black in comparison with the bright yellow CdS and white bare ZnO. Thus, in comparison to CdS, Ag_2S could more efficiently extend the absorption range of ZnO from UV to the entire visible region of the solar spectrum, giving it an edge over Cd-based sensitizers. Taking into consideration the efficient utilization of visible light in a large part of the solar spectrum, we envisage these core/shell nanostructures to possess practical interest as photocatalysts for the degradation of organic pollutants.

Photocatalytic Properties. The photodegradation of organic dye pollutants utilizing semiconductors is of paramount importance in environmental amelioration and portrays a commonly used approach to characterize the performance of photocatalysts. Toward this end, we have employed methylene blue (MB) as the evocative organic dye pollutant to explore the merits of ZnO/Ag_2S and ZnO/CdS core/shell nanostructures under illumination of visible light, and the results are presented in Figure 7. For pure ZnO nanorods, very poor photodegradation ability was observed under visible light illumination. However, the photodegradation of MB was appreciably enhanced on introducing core/shell nanostructures. To quantitatively explore the photocatalytic performances of these core/shell nanostructures, the corresponding photocatalytic reaction rate constants (k) of the MB degradation were computed by employing the equation

$$\ln(C/C_0) = kt \qquad (3)$$

on the basis of the pseudo-first-order model.[34] The enhanced photocatalytic performance of core/shell nanostructures in the photodegradation of MB could be ascribed to the extended light absorption and the type II band alignment.

Extended Light Absorption Range. The photocatalytic performance of a semiconductor is directly related to its light-harvesting ability, as it determines the generation of photocarriers responsible for the pollutant degradation. The extension of the absorption of ZnO to the visible region of the spectrum by the introduction of a core/shell geometry with the Ag_2S and CdS sensitizer already accounts for the dominance of the core/shell nanostructures in enhanced photocatalysis over the bare ZnO nanorods. As shown in Figure 6, there was a noticeable red shift of 70 nm (0.53 eV) and 100 nm (0.68 eV) in the absorption edge of ZnO in ZnO/CdS and ZnO/Ag_2S core/shell nanostructures, respectively. This observation points toward the more efficient light harvesting of the solar spectrum by the Ag_2S sensitizer by virtue of its narrow band gap, and thus the ZnO/Ag_2S core/shell nanostructures show a significant improvement in the degradation of MB in comparison to ZnO/CdS core/shell nanostructures under visible light illumination.

Type II Band Alignment. The superior photocatalytic performance of the core/shell nanostructures could also be justified by the relative alignments of the conduction and valence band positions of the core and shell components formed at the core/shell interface.

To understand the band alignment of core/shell nanostructures, we have calculated the band positions of the conduction and the valence band of ZnO/Ag_2S and ZnO/CdS core/shell nanorods using the equations[35]

Table 2. Optical and Photocatalytic Properties and Calculated CB and VB Positions of ZnO and ZnO/Ag_2S and ZnO/CdS Core/Shell Nanostructures

sample	shell thickness (nm)	absorption band (nm)	photocatalytic efficiency (%)	rate constant (min^{-1})	CB (eV)	VB (eV)	CB offset (eV)
ZnO		374	6.2	8.78×10^{-4} ($\pm 0.50 \times 10^{-4}$)	−0.36	2.95	
ZnO/Ag_2S	15	470	90.5	3.56×10^{-2} ($\pm 0.45 \times 10^{-2}$)	−0.36, −0.50	2.95, 0.90	0.14
ZnO/CdS	15	445	83.1	2.98×10^{-2} ($\pm 0.20 \times 10^{-2}$)	−0.36, −0.54	2.95, 1.93	0.18

$$E_{CB} = X - 0.5E_g + E_0 \tag{4}$$

$$E_{VB} = E_{CB} + E_g \tag{5}$$

where E_{CB} refers to the conduction band (CB) potential, E_{VB} refers to the valence band (VB) potential, E_g stands for the energy of the band gap of the semiconductor, X signifies the electronegativity of the semiconductor and could be manifested as the geometric mean of electronegativity of combining elements, and E_0 refers to the scaling factor describing the redox level of the reference electrode to the vacuum ($E_0 = -4.5$ eV for NHE). Using eqs 4 and 5, the calculated CB (E_{CB}) and VB (E_{VB}) positions for ZnO, Ag_2S, and CdS are given in Table 2. From the obtained CB and VB values of ZnO and Ag_2S and of ZnO and CdS, we have drawn the respective band alignment diagrams for the ZnO/Ag_2S and ZnO/CdS core/shell nanostructures (band gap energy of shell materials: Ag_2S or CdS is calculated from the absorption spectra as shown in Figure S3 (Suppporting Information)). The energies of the CB and VB of the shell components (in ZnO/CdS and ZnO/Ag_2S) are found to be higher than those of the core, which is a characteristic of the type II band gap configuration (Figure 8).

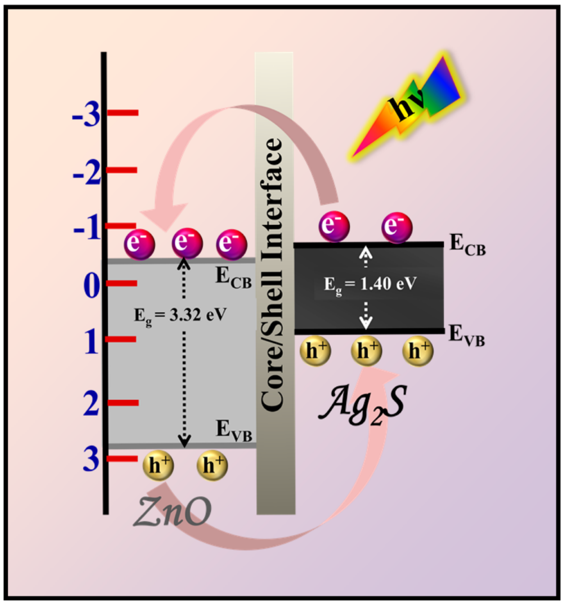

Figure 8. Schematic illustration of type II band alignment and the photogenerated charge transfer process in ZnO/Ag_2S core/shell nanostructures.

The type II core/shell structures have a band structure that results in a staggered band configuration at the core/shell interface where both CB and VB of the core are both either lower or higher than the shell. Photoexcited carriers would be preferably transferred through the interface and confined in different components of the nanostructures to manage the lowest energy states, ensuing in the tailoring of the relative positions of the electronic energy levels of the semiconductors to generate new band gaps. This alignment is the likely driving force for the increased photocatalytic activity of the core/shell nanostructures over their individual counterparts. Thus, the unique spatial distribution of the core-confined electron and shell-confined hole in type II core/shell nanostructures sanctions the efficient separation of the charge carriers, suggesting that they are ideal light harvesters for photovoltaic and photocatalytic applications.[36] However, the degree of charge separation within the type II core/shell nanostructures is strongly governed by the conduction band edge offset of the core and the shell materials. Using the band-alignment diagram (as presented in Figure 8), we have calculated offsets in conduction band minimum (CBM) of 0.14 and 0.18 eV in ZnO/Ag_2S and ZnO/CdS core/shell nanostructures, respectively. The results of optical and photocatalytic properties and calculated CB and VB positions of ZnO and ZnO/Ag_2S and ZnO/CdS core/shell nanorods are summarized in Table 2. The conduction band (CB) offset between ZnO and Ag_2S is small (in comparison to that for ZnO and CdS), which causes efficient photoinduced electron injection from the Ag_2S shell into the conduction band of ZnO, thus leading to enhanced photodegradation of the MB dye.

Thus, core/shell nanostructures of ZnO/Ag_2S offer enhanced photodegradation of methylene blue, as they take advantage of the improved light harvesting and small conduction band offset, allowing the efficient separation of photogenerated charge carriers.

Photocatalysis Mechanism. *Understanding the Role of Active Species.* The mechanism involving the semiconductor photocatalysis is well-understood. At the outset, under the illumination of visible light, with photon energy exceeding the band gap of the semiconductor, the photogenerated charge carriers electrons and holes are generated, which could be either trapped at defect sites or diffused toward the surface of the photocatalyst. These holes and electrons perform their independent reduction and oxidation reactions to produce active oxygen radical species, such as superoxide radical anion ($O_2^{\bullet -}$) and hydroxyl radicals ($OH^{\bullet}$), which then participate in photocatalytic degradation of organic pollutants in water. Therefore, a series of controlled experiments utilizing various radical scavengers has been carried out in order to deeply understand the role of active oxygen species involved in the photodegradation of MB deploying ZnO/Ag_2S core/shell nanostructures, which in turn gives further insight into elucidation of the photocatalysis mechanism. As the separation of electrons and holes is always identified to be the opening step in the photocatalytic degradation, we have first investigated the role of electrons and holes in the photocatalytic process.

Role of Electrons. To understand the role of photogenerated electrons in MB degradation, control experiments with and without the addition of $AgNO_3$ as an electron scavenger were carried out. As shown in Figure 9, the photocatalysis of MB over ZnO/Ag_2S core/shell nanostructures was remarkably

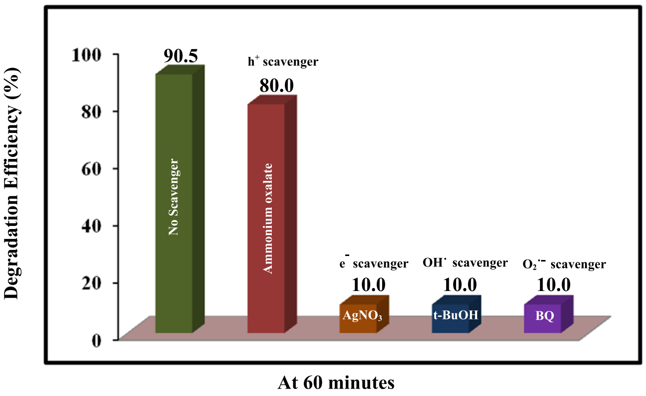

Figure 9. Controlled experiments using different active species scavengers for the photodegradation of MB over ZnO/Ag_2S core/shell nanostructures under illumination of visible light for 60 min.

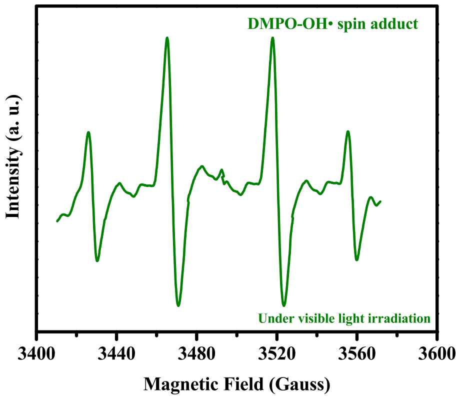

Figure 10. EPR spectra of DMPO adduct with $OH^{\bullet}$ photogenerated over ZnO/Ag_2S core/shell nanostructures under illumination of visible light.

retarded by 80% when $AgNO_3$ was introduced into the reaction system. This finding highlights the crucial role of photogenerated electrons in driving the photocatalytic degradation of MB.

Role of Holes. To unfold the role of photogenerated holes, ammonium oxalate (AO), a quencher for holes, was added to the MB solution. The reduction in photocatalytic efficiency of MB from 90 to 80% with the addition of ammonium oxalate points toward the insignificant role of holes either acting as the oxidizing agent or the originator of $OH^{\bullet}$ radicals in the MB degradation. After analyzing the role of photogenerated carriers, we move toward the role of active oxygen species generated through photogenerated carriers.

Role of Hydroxyl Radicals and Superoxide Radical Anions. To explore the role of $OH^{\bullet}$ and $O_2^{\bullet-}$ in the MB degradation, *t*-BuOH, an efficient $OH^{\bullet}$ quencher, and benzoquinone (BQ), a scavenger for $O_2^{\bullet-}$, were added. A decline in photocatalytic efficiency from 90 to 10% was observed in both cases, indicating the decisive role played by them. Thus, these results allow us to show that the oxidation of MB dye over ZnO/Ag_2S core/shell nanostructures proceeded by about 80% through the reaction with $OH^{\bullet}$, and the remaining 10% occurred via direct interaction with holes.

Detection of $OH^{\bullet}$ (Hydroxyl Radicals) and $O_2^{\bullet-}$ (Superoxide Anion Radicals) in ZnO/Ag_2S Core/Shell Nanostructures using EPR Spectroscopy. An EPR spin-trapping technique was adopted to further validate the generation of $OH^{\bullet}$ in the ZnO/Ag_2S core/shell nanostructures under illumination of visible light. DMPO, prevalent spin trap, recognizes the hydroxyl radicals ($OH^{\bullet}$) to produce the DMPO−$OH^{\bullet}$ adduct, which displays a quartet EPR signal. The DMPO can also trap superoxide radical anions ($O_2^{\bullet-}$) to generate the DMPO−$HO_2^{\bullet}$ adduct (comprised of a sextet EPR signal).

As portrayed in Figure 10, utilization of visible irradiation generated the 1:2:2:1 quartet EPR signal with the splitting parameters A_N = 13.9 G, A_H = 13.5 G, and g = 2.0063, characteristic for the DMPO−$OH^{\bullet}$ adduct.[37] Nevertheless, no signal corresponding to DMPO−$HO_2^{\bullet}$ spin adduct is seen for ZnO/Ag_2S core/shell nanostructures under illumination of visible light. Analogous experiments in the dark evince no signal, thus corroborating that the hydroxyl radicals are generated in ZnO/Ag_2S core/shell nanostructures under the application of visible light. Thus, the above findings faithfully endorse the controlled experiments using active species scavengers that $OH^{\bullet}$ is the ruling contributor engaged in the photodegradation of MB deploying ZnO/Ag_2S core/shell nanostructures.

With the information from the analysis of controlled experiments using active species scavengers, EPR spectroscopy, and band edge positions of core and shell components at hand, we propose a feasible photodegradation mechanism for the MB dye deploying ZnO/Ag_2S core/shell nanostructures, as illustrated below:

$$Ag_2S + h\nu \rightarrow Ag_2S(e^-{}_{CB}\cdots h^+{}_{VB})$$

$$Ag_2S(e^-{}_{CB}) + ZnO \rightarrow Ag_2S + ZnO(e^-{}_{CB})$$

$$O_2 + ZnO(e^-{}_{CB}) \rightarrow O_2^{\bullet-} + ZnO$$

$$O_2^{\bullet-} + H_2O \rightarrow HO_2^{\bullet} + OH^-$$

$$HO_2^{\bullet} + H_2O \rightarrow OH^{\bullet} + H_2O_2$$

$$H_2O_2 \rightarrow 2OH^{\bullet}$$

$$MB + OH^{\bullet} \rightarrow CO_2 + H_2O$$

$$MB + Ag_2S(h^+{}_{VB}) \rightarrow \text{degradation products}$$

where $e^-{}_{CB}$ signifies the conduction band electron and $h^+{}_{VB}$ stands for the valence band hole.

Upon visible light illumination, Ag_2S is band gap photoexcited, generating electron−hole pairs (ZnO being a wide band gap semiconductor cannot be photoexcited by visible irradiation). These electron−hole pairs are then separated; electrons move to the CB, leaving behind the same amount of holes in the VB. As also pointed out earlier, the energy of the CB of Ag_2S (−0.50 eV) is higher than that of ZnO (−0.36 eV), thus impelled by the decreased potential energy, the photogenerated electrons in CB of Ag_2S tended to transfer to that of ZnO and, in contrast, holes moved from the VB of ZnO toward that of Ag_2S, under illumination of visible light. As a result, the photoexcited electrons were localized in the core (ZnO), whereas holes were mainly localized in the shell (Ag_2S), which mitigated their probability of recombination and enabled them to drift toward the surfaces of ZnO and Ag_2S, respectively, to immediately join in the redox reactions, in which electrons reduce dissolved molecular oxygen to produce superoxide radical anions ($O_2^{\bullet-}$) while holes oxidize H_2O molecules to yield hydroxyl radicals ($OH^{\bullet}$).

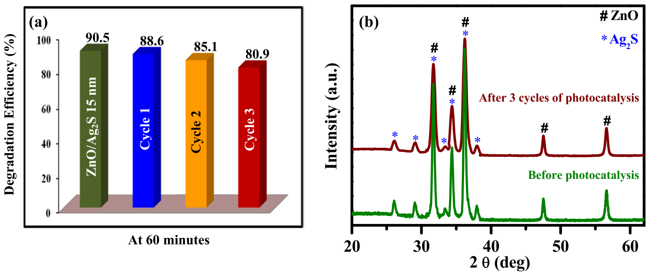

Figure 11. (a) Percent degradation efficiency of ZnO/Ag_2S core/shell nanostructures with increasing number of catalytic cycles and (b) PXRD patterns of ZnO/Ag_2S core/shell nanostructures before and after photocatalytic reactions.

Reusability of the ZnO/Ag_2S Core/Shell Photocatalyst. Keeping the superiority of ZnO/Ag_2S core/shell nanostructures in mind (over ZnO/CdS core/shell nanostructures), we have performed a recyclability test, which is a determinative factor for a photocatalyst to be of viable utilization in environmental applications.

To assess the recyclability performance of ZnO/Ag_2S core/shell nanostructures, we carried out three cycles of photocatalytic degradation of MB under illumination of visible light. As demonstrated in Figure S4 (Supporting Information) and Figure 11a, subsequent to further three photodegradation cycles of MB, the photocatalytic behavior of ZnO/Ag_2S core/shell nanostructures exhibited no significant loss in photoactivity. The efficiency of the core/shell nanostructures photocatalyst to degrade MB dye subsequent to the first, second, and third cycles was found to be 88.6(±2.1), 85.1(±1.9), and 80.9(±3.2)%, respectively (Figure 11a). The degradation efficiency of the photocatalyst is discerned to be curtailed only by 10% in the third cycle, which could stem from inescapable loss of the photocatalyst during the recovery process via centrifugation. The photostability of the ZnO/Ag_2S core/shell photocatalyst is also seen in the XRD data, which show no change in the diffraction pattern before and after the three cycles of photodegradation (as evident from Figure 11b).

To ensure that the photocatalyst is also morphologically stable even after three cycles of photodegradation, we have carried out FESEM observations. As can be seen from Figure S5 (Supporting Information), no noticeable difference in the morphology of the ZnO/Ag_2S core/shell photocatalyst is recognized even after three photocatalytic cycles. Thus, all these results of recyclability experiment on ZnO/Ag_2S core/shell nanostructures unambiguously support the premise that the system may be adopted as a practically viable and stable photocatalyst.

Thus, this work has been an attempt to develop efficient nontoxic alternatives to heavy-metal-containing nanostructures for environmentally friendly applications. Our results unveil the superiority of Ag_2S as sensitizer over Cd-based sensitizers in engineering the band gap of wide band gap semiconductors.

■ CONCLUSIONS

The idea of the present paper was to realize an efficacious strategy to engineer the band gap of ZnO nanomaterials and make them applicable for absorption of visible light. This idea was achieved to the fullest extent. We have demonstrated environmentally benign ZnO/Ag_2S core/shell nanostructures for enhanced light harvesting and visible-light photocatalysis. A combination of XRD, FESEM, TEM, HRTEM, EDS elemental mapping, and absorption studies has been used to support the formation of core/shell nanostructures. Sensitizing ZnO with Ag_2S resulted in substantially enhanced light absorption and degradation of MB under visible irradiation, in comparison to Cd sensitizers, owing to the narrow band gap of Ag_2S. Our findings are immensely significant owing to the following grounds. First, it enables us to design and develop environmentally benign core/shell photocatalysts for photodegradation of organic pollutants in water. Second, it suggests the possibility of using Ag_2S as an environmentally benign sensitizer that could supersede Cd-based sensitizers. Third, it allows us to potentially engineer the band gap of ZnO materials. We, therefore, expect our findings to bear vast potential toward the development of environmentally benign core/shell photocatalysts.

■ ASSOCIATED CONTENT

Ⓢ Supporting Information

Figures giving details of the synthesis of CdS and Ag_2S (shell materials), XRD patterns of shell materials (a) CdS and (b) Ag_2S, optical absorption spectra of shell materials (a) CdS and (b) Ag_2S, inset showing the band gap values of CdS and Ag_2S, recyclability of the photodegradation of MB for ZnO/Ag_2S core/shell nanostructures under visible light, and a FESEM image of ZnO/Ag_2S core/shell nanostructures after three photocatalytic cycles. This material is available free of charge via the Internet at http://pubs.acs.org.

■ AUTHOR INFORMATION

Corresponding Authors

*A.K.G.: e-mail, ashok@chemistry.iitd.ernet.in; tel, 91-11-26591511; fax, 91-11-26854715.
*S.K.: e-mail: sunita.iitd@gmail.com.

Notes

The authors declare no competing financial interest.

■ ACKNOWLEDGMENTS

The authors thank the Council of Scientific and Industrial Research, Government of India, for financial support.

■ REFERENCES

(1) Kamat, P. V. *J. Phys. Chem. C* **2007**, *111*, 2834.
(2) Yang, J.; Wang, D.; Han, H.; Li, C. *Acc. Chem. Res.* **2013**, *46*, 1900.
(3) Serpone, N.; Emeline, A. V. *J. Phys. Chem. Lett.* **2012**, *3*, 673.
(4) Lang, X.; Ma, W.; Chen, C.; Ji, H.; Zhao, J. *Acc. Chem. Res.* **2014**, *47*, 355.
(5) Xu, C.; Yang, W.; Guo, Q.; Dai, D.; Chen, M.; Yang, X. *J. Am. Chem. Soc.* **2013**, *135*, 10206.
(6) Roy, N.; Sohn, Y.; Pradhan, D. *ACS Nano* **2013**, *7*, 2532.
(7) Josephine, G. A. S.; Sivasamy, A. *Environ. Sci. Technol. Lett.* **2014**, *1*, 172.

(8) Boppella, R.; Anjaneyulu, K.; Basak, P.; Manorama, S. V. *J. Phys. Chem. C* **2013**, *117*, 4597.
(9) Xiao, F.–X. *ACS Appl. Mater. Interfaces* **2012**, *4*, 7055.
(10) Tiwana, P.; Docampo, P.; Johnston, M. B.; Snaith, H. J.; Herz, L. M. *ACS Nano* **2011**, *5*, 5158.
(11) Zhai, T.; Xie, S.; Zhao, Y.; Sun, X.; Lu, X.; Yu, M.; Xu, M.; Xiao, F.; Tong, Y. X. *CrystEngComm* **2012**, *14*, 1850.
(12) (a) Ansari, S. A.; Khan, M. M.; Ansari, M. O.; Lee, J.; Cho, M. H. *J. Phys. Chem. C* **2013**, *117*, 27023. (b) Fu, H.; Xu, T.; Zhu, S.; Zhu, Y. *Environ. Sci. Technol.* **2008**, *42*, 8064.
(13) Xia, Y.; Yang, P.; Sun, Y.; Wu, Y.; Mayers, B.; Gates, B.; Yin, Y.; Kim, F.; Yan, H. *Adv. Mater.* **2003**, *15*, 353.
(14) Wu, P.; Zhang, H.; Qian, Y.; Hu, Y.; Zhang, H.; Cai, C. *J. Phys. Chem. C* **2013**, *117*, 19091.
(15) Choi, H.; Kamat, P. V. *J. Phys. Chem. Lett.* **2013**, *4*, 3983.
(16) Etgar, L.; Moehl, T.; Stefanie, G.; Gickey, S. G.; Eychmüller, A.; Grätzel, M. *ACS Nano* **2012**, *6*, 3092.
(17) Wood, B. C.; Schwegler, E.; Choi, W. I.; Ogitsu, T. *J. Am. Chem. Soc.* **2013**, *135*, 15774.
(18) Calzia, V.; Malloci, G.; Bongiovanni, G.; Mattoni, A. *J. Phys. Chem. C* **2013**, *117*, 21923.
(19) Boix, P. P.; Larramona, G.; Jacob, A.; Delatouche, B.; Mora-Seró, I.; Bisquert, J. *J. Phys. Chem. C* **2012**, *116*, 1579.
(20) Luo, J.; Karuturi, S. K.; Liu, L.; Su, L. T.; Tok, A. L. Y.; Fan, H. J. *Sci. Rep.* **2012**, *2*, 451.
(21) Wang, Z.; Shakya, A.; Gu, J.; Lian, S.; Maldonado, S. *J. Am. Chem. Soc.* **2013**, *135*, 9275.
(22) Zhu, G.; Pan, L. K.; Xu, T.; Sun, Z. *ACS Appl. Mater. Interfaces* **2011**, *3*, 1472.
(23) Khan, Z.; Chetia, T. R.; Vardhaman, A. K.; Barpuzary, D.; Sastri, C. V.; Qureshi, M. *RSC Adv.* **2012**, *2*, 12122.
(24) Panthani, M. G.; Kurley, J. M.; Crisp, R. W.; Dietz, T. C.; Ezzyat, T.; Luther, J. M.; Talapin, D. V. *Nano Lett.* **2014**, *14*, 670.
(25) Zhang, Y.; Hong, G. S.; Zhang, Y. J.; Chen, G. C.; Li, F.; Dai, H. J.; Wang, Q. B. *ACS Nano* **2012**, *6*, 3695.
(26) Tsai, S. H.; Chang, H. C.; Wang, H. H.; Chen, S. Y.; Lin, C. A.; Chen, S. A.; Chueh, Y. L.; He, J. H. *ACS Nano* **2011**, *5*, 9501.
(27) Zhu, H.; Song, N.; Lian, T. *J. Am. Chem. Soc.* **2011**, *133*, 8762.
(28) Lo, S. S.; Mirkovic, T.; Chuang, C.-H.; Burda, C.; Scholes, G. D. *Adv. Mater.* **2011**, *23*, 180.
(29) (a) Bishop, L. M.; Yeager, J. C.; Chen, X.; Wheeler, J. N.; Torelli, M. D.; Benson, M. C.; Burke, S. D.; Pedersen, J. A.; Hamers, R. J. *Langmuir* **2012**, *28*, 1322. (b) Khanchandani, S.; Kundu, S.; Patra, A.; Ganguli, A. K. *J. Phys. Chem. C* **2012**, *116*, 23653.
(30) Lin, C. C.; Li, Y. Y. *Mater. Chem. Phys.* **2009**, *113*, 334.
(31) Sadhu, S.; Patra, A. *J. Phys. Chem. C* **2012**, *116*, 15167.
(32) Manna, L.; Scher, E. C.; Li, L.-S.; Alivisatos, A. P. *J. Am. Chem. Soc.* **2002**, *124*, 7136.
(33) Kim, S.; Fisher, B.; Eisler, H.-J.; Bawendi, M. *J. Am. Chem. Soc.* **2003**, *125*, 11466.
(34) Zhou, X. M.; Lan, J. Y.; Liu, G.; Deng, K.; Yang, Y. L.; Nie, G. J.; Yu, J. G.; Zhi, L. J. *Angew. Chem., Int. Ed.* **2012**, *51*, 178.
(35) Zhang, X.; Zhang, L. Z.; Xie, T. F.; Wang, D. J. *J. Phys. Chem. C* **2009**, *113*, 7371.
(36) Verma, S.; Kaniyankandy, S.; Ghosh, H. N. *J. Phys. Chem. C* **2013**, *117*, 10901.
(37) Gu, L.; Wang, J.; Cheng, H.; Zhao, Y.; Liu, L.; Han, X. *ACS Appl. Mater. Interfaces* **2013**, *5*, 3085.